



HAL
open science

Inverse identification of local stiffness across ascending thoracic aortic aneurysms

Solmaz Farzaneh, Olfa Trabelsi, Stéphane Avril

► **To cite this version:**

Solmaz Farzaneh, Olfa Trabelsi, Stéphane Avril. Inverse identification of local stiffness across ascending thoracic aortic aneurysms. *Biomechanics and Modeling in Mechanobiology*, 2019, 18 (1), pp.137-153. 10.1007/s10237-018-1073-0 . hal-02004232

HAL Id: hal-02004232

<https://hal.science/hal-02004232>

Submitted on 1 Feb 2019

HAL is a multi-disciplinary open access archive for the deposit and dissemination of scientific research documents, whether they are published or not. The documents may come from teaching and research institutions in France or abroad, or from public or private research centers.

L'archive ouverte pluridisciplinaire **HAL**, est destinée au dépôt et à la diffusion de documents scientifiques de niveau recherche, publiés ou non, émanant des établissements d'enseignement et de recherche français ou étrangers, des laboratoires publics ou privés.

INVERSE IDENTIFICATION OF LOCAL STIFFNESS ACROSS ASCENDING THORACIC AORTIC ANEURYSMS

Solmaz Farzaneh · Olfa Trabelsi ·
Stéphane Avril

the date of receipt and acceptance should be inserted later

Abstract Aortic dissection is the most common catastrophe of the thoracic aorta, with a very high rate of mortality. Type A dissection is often associated with an ascending thoracic aortic aneurysm (ATAA). However, it is widely acknowledged that the risk of type A dissection cannot be reliably predicted simply by measuring the ATAA diameter and there is a pressing need for more reliable risk predictors. It was previously shown that there is a significant correlation between a rupture criterion based on the ultimate stretch of the ATAA and the local membrane stiffness of the aorta. Therefore, reconstructing regional variations of the membrane stiffness across the aorta appears highly important. In this paper, we present a novel non-invasive inverse method to identify the patient-specific local membrane stiffness of aortic walls based on preoperative gated CT scans. Using these scans, a structural mesh is defined across the aorta with a set of nodes attached to the same material points at different time steps throughout the cardiac cycle. For each node, time variations of the position are analyzed using Fourier series, permitting the reconstruction of the local strain distribution (fundamental term). Relating these strains to tensions with the membrane stiffness, and writing the local equi-

S. Farzaneh · O. Trabelsi · S. Avril*

Mines Saint-Étienne, CIS-EMSE, F-42023 Saint-Étienne, France

INSERM, U1059, SAINBIOSE, F-42023 Saint-Étienne, France

Université de Lyon, F-69000 Lyon, France

*Corresponding author E-mail: avril@emse.fr

librium satisfied by the tensions, the local membrane stiffness is finally derived at every position. The methodology is applied onto the ascending and descending aorta of three patients. Interestingly, the regional distribution of identified stiffness properties appears heterogeneous across the ATAA. Averagely, the identified stiffness is also compared with values obtained using other non-local methodologies. The results support the possible non-invasive prediction of stretch-based rupture criteria in clinical practice using local stiffness reconstruction.

Keywords Non-invasive inverse method · Local membrane stiffness · Finite-elements · Ascending thoracic aortic aneurysms · Patient-specific · Risk of rupture

1 Introduction

Ascending thoracic aortic aneurysms (ATAAs) manifest by localized ballooning of the aorta. They are difficult to detect because they usually have no symptom. Unrecognized and untreated TAA may lead to dissection or rupture of the aneurysm ending with instantaneous death. Independently of age and gender, about 30,000 people in Europe and 15,000 people in the United States are diagnosed with a TAA every year [5, 31, 42].

ATAA are commonly treated with a timely surgical repair by replacement of the dilated aortic segment with synthetic grafts. For patients without any familial disorders such as Marfan syndrome, elective surgical intervention of ATAA is recommended when its diameter is larger than 5.5 cm or when it is considered as a fast growing aneurysms (growth > 1 cm per year) [6, 8, 9, 15, 31]. The diameter of 5.5 cm as a criterion for decision-making of surgical intervention is extensively recognized as an insufficient criterion. For example, the International Registry of Acute Aortic Dissection (IRAD) conveyed that among 591 type "A" aortic dissections, 59% had a diameter below 5.5 cm. Moreover, several studies considering abdominal aortic aneurysm (AAA) suggest that biomechanical factors may reliably predict the risk of rupture rather than the diameter criterion alone [17, 20, 14]. Wall stress analysis and identification of patient-specific material properties of abdominal aortic aneurysms using 4D ultrasound were performed to improve rupture risk assessment [49]. It is well-known that the rupture of ATAA occurs when

22 the stress applied to the aortic wall reaches the rupture stress [34,36,47]. Another
23 definition of rupture can be represented when the stretch applied to the tissue
24 is greater than its maximum extensibility or distensibility (stretch based rupture
25 criterion). Accordingly, Duprey et al. [13] proposed a stretch-based rupture risk
26 criterion and showed its correlation with tangent elastic modulus in ATAA based
27 on data collected in 31 patients. In that study, individual rupture stretch and tan-
28 gent elastic modulus were determined in vitro by means of bulge inflation tests on
29 the identical ATAA wall tissue segments that had been excised intraoperatively.
30 Trabelsi et al. [48] proposed a method for the in vivo identification of the (global)
31 stiffness of an aortic segment based on the determination of volumetric distensibil-
32 ity from gated CT scans and pulse pressure. However, only moderate correlation
33 was found between the global in vivo stiffness values and the (local) stretch based
34 rupture risk criterion determined from bulge inflation tests on excised tissue seg-
35 ments of 13 ATAA. Therefore, the assessment of the local elastic properties of the
36 ATAA-wall from in vivo data that are clinically available, might be a crucial point
37 for establishing a reliable method of estimation of ATAA rupture risk [39]. In the
38 present paper, a new inverse approach to this task is presented.

39 This is meaningful as stiffening of the aortic wall is both a cause and a conse-
40 quence of ATAA [7,50]. Stiffening leads to a decrease of extensibility due to loss
41 of elastin and deposition of collagen during growth and remodeling. There are
42 studies that have indeed demonstrated such stiffening (without wall weakening)
43 in age-matched subjects [30,19]. They mostly found local variations of mechanical
44 parameters along the longitudinal direction, indicating higher strength and peak
45 elastic modulus along the circumferential direction compared to the longitudinal
46 direction [30]. Therefore, identifying non-invasively the *in vivo* elastic properties
47 of the aorta would help clinicians to take decisions whether the patient needs
48 surgical intervention. Besides, the mechanical properties can be used to perform
49 computational analyses, the accuracy of which will rely on the accuracy of input
50 parameters.

51 However, non-invasive characterization of elastic properties is not the most
52 common approach for deriving material properties of aortas. The most common
53 methods to obtain material properties are *in vitro* uniaxial and biaxial mechanical
54 tests [7,21,40]. They permit plotting stress-strain curves and deriving parameters

55 of strain energy functions or linearized elastic moduli of the aneurysmal walls at
56 different stages of loading [50]. Several studies have characterized the mechanical
57 properties of ATAA via strain energy functions and elastic moduli indicating that
58 ATAA causes stiffening and extensibility reduction of tissue while having no effect
59 on strength reduction. To assess rupture risk on a patient-specific level, their
60 results imply decreased tissue compliance as a rupture risk factor [46,35].

61 To our best knowledge no study has ever identified regional variations of mate-
62 rial properties in ATAAs on a patient-specific basis using a non-invasive methodol-
63 ogy. Therefore, the main objective of this work is to present a novel methodology
64 based on gated CT images for the identification of local stiffness properties in
65 ATAAs under assumptions of linearized and isotropic elasticity. After a compre-
66 hensive presentation, we show exemplary results on three patients for the proof of
67 concept.

68 **2 Material and methods**

69 **2.1 Origin of data**

70 After informed consent and according to a protocol approved by the Institutional
71 Review Board of the University Hospital Center of Saint-Etienne, non invasive
72 systolic and diastolic blood pressures in brachial artery and gated CT scans were
73 obtained for three patients who underwent elective surgical repair of ATAA at
74 the University Hospital of Saint-Etienne (CHU-SE) in France. The demographic
75 information of these patients is recorded in Table 1. For each patient, images were
76 recorded at ten phases of their cardiac cycle. These images were used to reconstruct
77 the geometry of their whole aorta, including diastolic and systolic phases. Semi-
78 automatic segmentation of the CT image slices was done using MIMICS (v.10.01,
79 Materialise NV). The three-dimensional (3D) surface of the aorta was generated
80 for each phase and exported as STL format. All phases were cut by the same cross
81 sectional planes to predefine a domain of the aorta larger than the final segment
82 of interest in both ascending and descending parts. The purpose was to initiate
83 the procedure in order to run the Vascular Modeling Toolkit (VMTK, Orobix,
84 Bergamo, Italy; www.vmtk.org) [1] and to derive the parametric coordinates of

85 the surface. Identical smoothing factor was applied at all phases. To recognize the
 86 systolic and diastolic phases, the luminal volumes of all phases were compared.
 87 The systolic scan was defined as the one with the largest volume and the diastolic
 88 scan as the one with the smallest volume. See Fig. 1 in which each phase is shown
 89 using a different color.

90 2.2 Theory of the inverse approach

91 A set of nodes was defined across each reconstructed aortic geometry, with the
 92 requirement that a node represented the position of the same material point at each
 93 phase of the cardiac cycle. For this, it was essential to reconstruct a structural mesh
 94 for all phases with an identical number of elements and nodes and to have a mesh
 95 morphing function between the geometries of each phase. The structural mesh
 96 was convenient for several reasons; 1- to compare information of each element and
 97 nodes in identical position between different phases, 2- to reduce the computational
 98 time, 3- structural mesh generally deforms under lower strain energy states.

99 VMTK [1] was employed to generate the structural mesh from STL files. The
 100 method was based on centerlines and decomposition of the surface into existing
 101 branches and mapping each branch onto template parametric coordinates. Once
 102 a bifurcation is split into branches, each branch is topologically equivalent to a
 103 cylinder and can be mapped onto a set of rectangular parametric coordinates [1].
 104 The approach for mapping the surface of bifurcations consisted of several steps:
 105 calculation of centerlines, definition of the reference system, decomposition of the
 106 bifurcation into its branches and their parameterization. VMTK provides a tech-
 107 nique based on objective criteria capable of generating consistent parameteriza-
 108 tions over a wide range of bifurcating geometries. Let $\partial\Omega_i$ be the surface of the
 109 i th branch which is delimited by two topological circles ψ_{i0} and ψ_{iL} . Considering
 110 $u \in [0, L_i]$ is the longitudinal parametric coordinate and $v \in [-\pi, \pi]$ is the peri-
 111 odic circumferential parametric coordinate, over the parametric space of $U \subset \mathbb{R}^2$
 112 in the coordinates $U = (u, v)$, a bijective mapping is derived as [1]

$$\Phi : \underset{\mathbf{x}}{\partial\Omega_i} \rightarrow \underset{\mathbf{u}}{U} \quad (1)$$

113 such that $\Phi(\mathbf{x}) = (0, v)$ on ψ_{i0} and $\Phi(\mathbf{x}) = (L_i, v)$ on ψ_{iL} . Longitudinal mapping
 114 in VMTK is created by a harmonic and a stretch function to achieve localization
 115 with respect to centerline abscissa and reference system [23]. The harmonic function
 116 $f = f(\mathbf{x})$ with $\mathbf{x} \in \partial\Omega_i$ is computed by solving the elliptic partial differential
 117 equation as

$$\Delta_B f = 0 \quad (2)$$

118 where Δ_B is the Laplace-Beltrami operator. The longitudinal parametric coordi-
 119 nate is expressed by

$$u(\mathbf{x}) = s \circ f(\mathbf{x}) \quad (3)$$

120 where s is the stretch function and can be defined as

$$s(f) = \frac{1}{|\lambda(f)|} \int_{\lambda(f)} g(\mathbf{x}) d\lambda \quad (4)$$

121 where $\lambda(f)$ indicates a level-set of f . The angular position of each node is de-
 122 termined by a set of normals along the curve of frame τ , named $\mathbf{n}(\tau)$ (which is
 123 directed towards the center of the osculating circle of the curve at each point), and
 124 its nearest point on the centerline, $\mathbf{c}(\tau)$, as

$$v(\mathbf{x}) = \arccos((\mathbf{x} - \mathbf{c}(\tau)) \cdot \mathbf{n}(\tau)) \quad (5)$$

125 where τ indicates the different time frames.

126 One of the requirements is that the inlets and outlets of the imported mesh into
 127 VMTK should be open. Left subclavian artery, brachiocephalic artery, left com-
 128 mon carotid artery and coronary artery branches were used to provide anatom-
 129 ical references to ensure that the measurements taken at different phases of the
 130 cardiac cycle were at the same location in the aorta (see Fig. 1). Eventually,
 131 the extracted data from VMTK were postprocessed in Matlab to extract an ac-
 132 curate mesh using the longitudinal and circumferential metrics obtained from
 133 VMTK. A template meshgrid with an arbitrary number of points was created
 134 in the $u_{\text{temp}} \in [u_{\text{min}}, u_{\text{max}}]$ and $v_{\text{temp}} \in [-\pi, \pi]$ domain. A polynomial ap-
 135 proximation was implemented around each node of the template meshgrid. For
 136 instance, let $(u_{\text{temp}}^i, v_{\text{temp}}^i)$ denote the parametric coordinates of node \mathbf{X}_i . Let
 137 $(\mathbf{u}_{\text{nb}}, \mathbf{v}_{\text{nb}})$ be the parametric coordinates of the nodes of the reconstructed STL
 138 surface around \mathbf{X}_i . These nodes were selected such that $du_j = (u_{\text{nb}}^j - u_{\text{temp}}^i) < \delta_u$

139 and $dv_j = (v_{nb}^j - v_{temp}^i) < \delta_v$, δ_u and δ_v defining the size of the neighborhood. We
 140 assumed $\delta_u=8$ mm and $\delta_v=\pi/5$ rad. Therefore using the least-squares method,
 141 the polynomial approximation was written such as

$$\mathbf{A}\mathbf{X} = \mathbf{X}_{nb} \quad (6)$$

142 with

$$\mathbf{A} = \begin{bmatrix} 1 & du_1 & dv_1 & du_1dv_1 & du_1^2 & dv_1^2 & du_1^2dv_1 & du_1dv_1^2 \\ \vdots & \vdots \\ 1 & du_k & dv_k & du_kdv_k & du_k^2 & dv_k^2 & du_k^2dv_k & du_kdv_k^2 \\ \vdots & \vdots \\ 1 & du_n & dv_n & du_ndv_n & du_n^2 & dv_n^2 & du_n^2dv_n & du_ndv_n^2 \end{bmatrix} \quad (7)$$

144

$$\mathbf{X} = \begin{bmatrix} X_1 & Y_1 & Z_1 \\ X_2 & Y_2 & Z_2 \\ \vdots & \vdots & \vdots \\ X_8 & Y_8 & Z_8 \end{bmatrix} \quad (8)$$

145 and

$$\mathbf{X}_{nb} = \begin{bmatrix} X_{nb}^1 & Y_{nb}^1 & Z_{nb}^1 \\ \vdots & \vdots & \vdots \\ X_{nb}^k & Y_{nb}^k & Z_{nb}^k \\ \vdots & \vdots & \vdots \\ X_{nb}^n & Y_{nb}^n & Z_{nb}^n \end{bmatrix} \quad (9)$$

146 **Based on a mesh sensitivity analysis, an average mesh size of 1×1 mm was used.**
 147 According to Wittek et al [52] who observed that the ascending thoracic aorta
 148 experiences clockwise and counterclockwise twist, we derived the time variations
 149 of the circumferential coordinate, v , of coronary arteries in the space of parametric
 150 coordinate and subtracted this value from the circumferential coordinate of the
 151 assumed reference phase in order to apply torsion during aortic wall motion. To
 152 adjust all phases longitudinally, the origin of u was set in the coronary plane
 153 at each phase. Accordingly, the torsion was applied by subtracting the shift of

154 the v value at the inlet, and by subtracting a shift in the v value all along the
 155 thoracic aorta, varying linearly from v to 0 between the inlet and the position of
 156 the brachiocephalic artery.

157 Any periodic function (in this case nodal coordinates of all phases, $x(t)$) can
 158 be expressed as a weighted sum of infinite series of sine and cosine functions
 159 of varying frequency. Therefore, having the structural mesh of all ten phases, a
 160 discrete Fourier transform was employed such as

$$x(t) = a_0 + \sum_{n=1}^{\infty} \left(a_n \cos(nft) + b_n \sin(nft) \right) \quad (10)$$

161 Where a_0 is the Direct Current (DC) term and the sum is the fundamental mag-
 162 nitude of the time-varying node positions when $n=1$ while f is the fundamental
 163 frequency. A strain analysis was performed on the average geometry (defined by
 164 using the DC terms of all nodal positions) by applying displacements (including
 165 torsion) at each node corresponding to the fundamental term obtained from the
 166 Fourier transform in Eq. 10. As the fundamental term is complex, the real and
 167 the imaginary parts are applied separately at the corresponding nodes (in their
 168 average position, defined by the DC term) using the finite element method (FEM).
 169 Eventually the reconstructed strain components were also complex. The compo-
 170 nents in the longitudinal and circumferential directions were derived respectively
 171 as

$$\begin{aligned} \varepsilon_1^{\text{com}} &= \varepsilon_1^r + i\varepsilon_1^{\text{im}} \\ \varepsilon_2^{\text{com}} &= \varepsilon_2^r + i\varepsilon_2^{\text{im}} \end{aligned} \quad (11)$$

172 where superscripts "r" and "im" indicate real and imaginary contributions, respec-
 173 tively. Therefore the magnitude of strains in the longitudinal and circumferential
 174 directions can be respectively obtained as

$$\begin{aligned} \varepsilon_1 &= \sqrt{\varepsilon_1^{r^2} + \varepsilon_1^{\text{im}^2}} \\ \varepsilon_2 &= \sqrt{\varepsilon_2^{r^2} + \varepsilon_2^{\text{im}^2}} \end{aligned} \quad (12)$$

175 The results of the strain computation are independent of the chosen material
 176 properties and this methodology is applicable to finite deformation problems. Al-
 177 though the aortic tissue is globally anisotropic and nonlinear, we linearized here
 178 its mechanical behaviour in the range of strains induced by pressure variations
 179 between diastole and systole, and neglected anisotropic effects in this range too.

180 The constitutive equations reduced to Hooke's law in plane stress. **Due to the spa-**
 181 **tial resolution of CT, the local aortic thickness cannot be measured accurately in**
 182 **vivo. The thickness was previously measured in vitro on the excised sample after**
 183 **the surgery [13]. However, the in vitro measurement is performed when the tissue**
 184 **is loadfree, whereas the tissue is stretched and pressurized in vivo. Therefore the**
 185 **thickness can vary significantly *in vivo*, thus to express the Hooke's law, we wrote**
 186 the membrane tensions, τ , as

$$\begin{aligned}
 \tau_1(t) &= \tau_1^0 + Q(\varepsilon_1(t) + \nu\varepsilon_2(t)) \\
 \tau_2(t) &= \tau_2^0 + Q(\nu\varepsilon_1(t) + \varepsilon_2(t))
 \end{aligned}
 \tag{13}$$

187 where τ_1^0 and τ_2^0 are the DC terms of both components of the membrane tension
 188 (representing pretensions existing in the average geometry due to average blood
 189 pressure and axial tension), Q is the membrane stiffness and ν is the Poisson's
 190 ratio in which incompressibility is assumed ($\nu=0.49$). We derived τ_1^0 and τ_2^0 by
 191 achieving an FE stress analysis on the average geometry under the effect of the
 192 average pressure P_0 using the approach proposed by [32].

193 As shown in Fig. 2 it is assumed that each element of the arterial wall is a
 194 finite sector of an ellipsoidal membrane with radii r_1 and r_2 in both circumferen-
 195 tial and longitudinal directions. So, in the framework of these assumptions, local
 196 equilibrium equations can be written as

$$P(t) = \frac{\tau_1(t)}{r_1(t)} + \frac{\tau_2(t)}{r_2(t)}
 \tag{14}$$

197 where r_1 and r_2 are the radii of the element sector in both directions (major and
 198 minor) as shown in Fig. 2 and P is the applied pressure. Using P_0 to denote the
 199 DC term of pressure variations, and neglecting second order variations, Eq. 14 can
 200 be rewritten:

$$\begin{aligned}
 P(t) - P_0 &= \frac{\tau_1(t) - \tau_1^0}{r_1^0} + \\
 &\frac{\tau_2(t) - \tau_2^0}{r_2^0} - \frac{\tau_1^0(r_1(t) - r_1^0)}{(r_1^0)^2} - \frac{\tau_2^0(r_2(t) - r_2^0)}{(r_2^0)^2}
 \end{aligned}
 \tag{15}$$

201 Using ΔP , $\Delta\tau_1$, $\Delta\tau_2$, Δr_1 and Δr_2 to denote the fundamentals of pressure, the
 202 circumferential and longitudinal components of the local tension tensor, and the
 203 circumferential and longitudinal radius of curvature, respectively, Eq. 15 can be
 204 written as follows:

$$\Delta P = \frac{\Delta\tau_1}{r_1^0} + \frac{\Delta\tau_2}{r_2^0} - \frac{\tau_1^0(\Delta r_1)}{(r_1^0)^2} - \frac{\tau_2^0(\Delta r_2)}{(r_2^0)^2} \quad (16)$$

205 In the following, we assume $\Delta P = (P_{sys} - P_{dias})/2$.

206 Substituting Eqs. 13 in 16, we obtain the membrane stiffness for each element
207 such as

$$Q = \frac{\Delta P + \frac{\tau_1^0 \Delta r_1}{(r_1^0)^2} + \frac{\tau_2^0 \Delta r_2}{(r_2^0)^2}}{\frac{\varepsilon_1(t) + \nu \varepsilon_2(t)}{r_1^0} + \frac{\nu \varepsilon_1(t) + \varepsilon_2(t)}{r_2^0}} \quad (17)$$

208 To obtain r_1 and r_2 fast and efficiently, we developed a method based on the
209 principle of virtual work as previously introduced in [4], so assuming stresses σ at
210 equilibrium with external loads \mathbf{T} should satisfy the following equation:

$$\int_v \sigma_{ij} : \varepsilon_{ij}^* dv + \int_{\partial v} T_i u_i^* ds = 0 \quad (18)$$

211 Where v and s are the volume and surface of the domain of interest, respectively, \mathbf{u}^*
212 is a virtual continuous displacement field and ε^* are the virtual strains related to
213 the gradients of the virtual displacements. As this equation is valid for any virtual
214 field, \mathbf{u}^* can be defined as a unit vector oriented along the normal directions of the
215 aortic wall at every node (directions $n_{1,2,3,4}^n$ in Fig. 2). Accordingly, it is possible
216 to derive the following local equation:

$$\sigma_1 h \varepsilon_1^* + \sigma_2 h \varepsilon_2^* = p u^* \quad (19)$$

217 Where σ_1 and σ_2 are the principal components of the stress and h is the thickness.
218 The Laplace law may be written:

$$\frac{\sigma_1}{r_1} h + \frac{\sigma_2}{r_2} h = p \quad (20)$$

219 By identification between the two previous equations, we obtain directly a relation-
220 ship between the local radii of curvature and the virtual strain fields. We applied
221 a displacement with arbitrary magnitude of u^* in the normal directions to each
222 node (directions $n_{1,2,3,4}^n$ in Fig. 2) to inflate virtually the aorta. After recording ε_1^*
223 and ε_2^* in the longitudinal and circumferential directions induced by this virtual
224 inflation, the radii can be calculated as

$$\frac{1}{r_1} = \frac{\varepsilon_1^*}{u^*} \quad (21)$$

$$\frac{1}{r_2} = \frac{\varepsilon_2^*}{u^*}$$

225 In this work we introduce the concept of "extensional stiffness" which equals the
226 material stiffness times the thickness and whose dimension is MPa.mm.

227 Stiffness variations across the different regions of the thoracic aorta may exist
228 at different scales. In order to filter out high frequency variations, the obtained
229 results were eventually fitted using Fourier polynomial of order 4 along the circum-
230 ferential directions and polynomials of order 3 along the axial direction, permitting
231 a smoother estimation of stiffness distribution.

232 2.3 Numerical implementation

233 In the current work we reconstructed ascending and descending aortas excluding
234 all branches. Therefore, the right coronary and brachiocephalic arteries were used
235 as reference points to obtain identical parts of the ascending aorta at different
236 phases and the left subclavian artery was used as a reference point to consider
237 identical parts of the descending aorta at different phases. For each patient and
238 each phase, a structural mesh using quadrilateral elements with four nodes was
239 prepared and then the average structural meshes of ascending and descending
240 aortas were obtained by averaging the nodal positions throughout the cardiac
241 cycle. Afterwards, for each aorta, the Abaqus FE software [24] was employed to
242 calculate ε_1^* and ε_2^* by applying u^* at each node in normal directions of $n_1^n:n_4^n$ in
243 Fig. 2. Moreover, two other independent FE analyses were performed by applying
244 corresponding real and imaginary displacements at each node (including aorta
245 torsion) to calculate $\varepsilon_1^{\text{com}}$ and $\varepsilon_2^{\text{com}}$ and subsequently ε_1 and ε_2 expressed in Eq. 12.
246 For each FE analysis, orientation user subroutine (ORIENT) was employed to
247 assign local material directions in order to save results in the local coordinate
248 system. Each geometry was a non-perfectly cylindrical geometry so that the radial
249 direction (normal to the artery) was defined as the outward normal direction to
250 each element, the axial direction was defined as the direction parallel to the luminal
251 centerline in the direction of the blood flow, and the circumferential direction was
252 perpendicular to both previously defined directions. To calculate and visualize the
253 local membrane stiffness expressed in Eq. 17, a user material subroutine (UMAT)
254 and a user-defined external databases (UEXTERNALDB) were coupled with the

commercial FE software Abaqus [24]. The complete methodology is summarized in a flowchart shown in Fig. 3.

In this work, we had to perform several different steps to characterize the local aortic stiffness for each patient. The most time consuming step was the segmentation of CT images (cleaning could last one day for the noisiest). Generation of the structural mesh took about 10 minutes including VMTK and further processing. It took less than 2 hours to prepare the ABAQUS input files for stress analyses, strain analyses, stiffness assessment and reconstruction. Each ABAQUS resolution took about five minutes.

3 Results

3.1 Numerical validation

Numerical validation was performed considering two different material behaviors; linear elastic and non-Linear anisotropic material properties.

3.2 Linear elastic material property

For the sake of validation, we used a reference aortic geometry (RG) and we created numerically a deformed aortic geometry (DG) by considering the effects of an average intramural pressure ($P=40$ mmHg (5.33 KPa)) onto the aorta modeled with a linear elastic behavior. The DG was derived by a finite element analysis using the raw STL mesh of the reference geometry. Two analyses (cases) were performed: one with a homogeneous stiffness in the whole aorta and another one with a heterogeneous stiffness distribution in which three regions were defined in the aorta, each one with different stiffness shown in Fig. 6. Each analysis provided a deformed STL mesh. Displacement maps used to reconstruct DG are shown in Fig. 4. Having in hand RG and DG for both cases, we performed our approach using VMTK and MATLAB to independently generate the structural mesh of each geometry. For the sake of validation, we subtracted the nodal coordinates

282 of both structural meshes (on RG and DG). As it can be observed in Fig. 5,
 283 we found a good agreement between the displacements reconstructed using our
 284 approach and the reference displacement, indicating that structural meshes of both
 285 geometries are related to nearly similar material points. After this first validation
 286 on the reconstructed displacement data, we applied the whole methodology with
 287 reconstruction of stiffness distributions from the two simulated cases. For each case,
 288 a stiffness distribution was obtained and compared to the reference one (Fig. 6).
 289 The reconstructed stiffness was in good agreement with the reference and especially
 290 the local heterogeneity could be well retrieved for the heterogeneous case. Artifacts
 291 only appear very locally at the proximal and distal parts of the aortic segment due
 292 to spurious effects of polynomial smoothing close to the boundary (edge effects).

293 3.3 Non-linear anisotropic material property

294 We have performed a complementary validation of our methodology considering
 295 anisotropy and effects of nonlinearity. We used the same aortic geometry (raw
 296 stl) as the one used for the linearized case study, which is the aortic geometry
 297 of a real patient which was segmented from a CT scan obtained at $P_{diastole}=80$
 298 mmHg (10.66 KPa). We modeled the aortic wall with a Gasser-Ogden-Holzapfel
 299 anisotropic strain energy function which may be written as [26]

$$\bar{\Psi} = C_{10}(\bar{I}_1 - 3) + \frac{k_1}{2k_2} \sum_{i=4,6} \left[\exp[k_2(\bar{I}_i - 1)^2] - 1 \right] + \kappa(J - 1)^2 \quad (22)$$

300 where C_{10} and k_1 are material parameters and have a stress-like dimension, and k_2
 301 is a dimensionless material parameters while κ is bulk modulus and J is Jacobian
 302 (local volume ratio). $\bar{I}_1 = tr(\bar{C})$, $\bar{I}_4 = \bar{C} : a_{01} \otimes a_{01}$ and $\bar{I}_6 = \bar{C} : a_{02} \otimes a_{02}$ are
 303 first, fourth and sixth invariants of the modified counterparts of the right Cauchy-
 304 Green tensor, \bar{C} . Note that the families of collagenous fibers are characterized by
 305 the two reference direction vectors $a_{0j} = [0 \cos\theta_j \sin\theta_j]$, $j = 1, 2$, with $|a_{0j}| = 1$.
 306 θ_j is the angles between the collagen fibers (arranged in symmetrical spirals) and
 307 the circumferential direction.

308 Two analyses were performed: One with a homogeneous distribution of hyperelas-
 309 tic material properties in the whole the aorta and the other with a heterogeneous
 310 distribution of hyperelastic material properties, considering three regions. Material

parameters used for this validation study are reported in Table 2. Before applying these two models to calculate displacement between diastole and systole, we first computed the zero pressure geometry in each case using the approach presented by Mousavi et al [38,39]. Afterwards, we calculate the deformation of the aortic geometry for a systolic pressure directly by applying $P_{systole}=120$ mmHg (16 KPa) onto the zero pressure geometry.

Having in hand the diastolic geometry and the computed systolic geometry, we ran our approach using VMTK and MATLAB to independently generate the structural mesh of each geometry (systolic and diastolic) in both homogeneous and heterogeneous analysis. We subtracted the nodal coordinates of both structural meshes (systolic and diastolic phases) to obtain the displacements between systole and diastole for each case. Assuming the diastolic phase as the reference geometry we applied our methodology to retrieve the stiffness of aorta. The identified results shown in Fig. 7 demonstrate that our methodology is able to retrieve the "stiff" region in the heterogeneous case, whereas the homogeneous case show only small variations which are mostly related to edge effects. However, this remains a qualitative comparison as the obtained linearized stiffness is not directly related to hyperelastic properties. This qualitative validation completes well the previous quantitative validation where we modeled the aorta with a linear elastic behavior and where we were able to retrieve the correct stiffness properties.

3.4 Patient-specific results

The methodology described previously was applied on 3 patients. The membrane stiffness of their aorta was reconstructed at every Gauss point of the mesh (excluding the branches and the region of the arch between the brachiocephalic and the left subclavian arteries) and then the values were interpolated at nodal positions. The results were plotted as independent colormaps which are shown in Fig. 8. The distributions appear heterogeneous, especially in the ATAA regions where some regions of relatively higher membrane stiffness appear. The distribution of local membrane stiffness showed higher values for ascending aortas compared to descending aortas.

341 3.5 Comparison of the results

342 For these 3 patients, elastic properties of their ATAA were previously characterized
 343 with two other methods:

- 344 1. An ATAA segment was defined by two transverse planes located respectively
 345 at 10 cm and 55 cm from the coronary artery. **Across the defined segment, the**
 346 **average distensibility of the ascending thoracic aorta was assessed from CT**
 347 **scans according to [48]**

$$D_V = \frac{\Delta V}{V \Delta P} \quad (23)$$

348 **Where V , ΔV and ΔP are respectively the luminal volume, the volume differ-**
 349 **ence between diastole and systole and the pressure difference.** The membrane
 350 stiffness was deduced as the ratio between the distensibility and the average
 351 diameter of the segment. Let $E_{in-vivo}$ denote the membrane stiffness obtained
 352 with this method.

- 353 2. After the surgical intervention on these patients, an ATAA segment was ex-
 354 cised. From this segment, a square ($45 \times 45 \text{ mm}$) was cut in the outer curvature
 355 region and tested in bulge inflation. The stress-strain response of the tested
 356 sample was linearized over a range of pressures inducing similar tensions in
 357 the tissue as the tensions produced by diastolic and systolic pressures. The
 358 obtained linearized stiffness of the tissue over this range, multiplied by tis-
 359 sue thickness, yielded another estimate of the membrane stiffness, which was
 360 denoted $E_{in-vitro}$.

361 Therefore, for each patient, we focused on the distribution of membrane stiffness
 362 across the ATAA segment and across the cut square (Fig. 9). For the sake of
 363 statistical analysis, we derived the median and interquartile ranges of all nodal
 364 values of the identified membrane stiffness (Fig. 10). The analysis was achieved
 365 first by taking all the values of the ascending aorta, then only the values in the
 366 ATAA segment and finally only the values of the cut square. For each patient, we
 367 also plotted in Fig. 10 the $E_{in-vitro}$ and $E_{in-vivo}$ values obtained by [13] and
 368 [48], respectively. This analysis showed that the median and interquartile values
 369 for different cuts of all patients are relatively at the same ranges. Comparing the
 370 interquartile box obtained in this study with the corresponding results of [48],

371 it can be deduced that for all patients $E_{in-vivo}$ is a value between the lower
372 and the median value (mostly close to median) while $E_{in-vitro}$ values are close
373 to lower corresponding interquartile. This can be explained by the mechanical
374 actions of surrounding tissues and environment *in vivo*, which may apply a counter
375 pressure on the artery. We did not take into account this counter pressure in the
376 identification as $P(t)$ in Eq. 14.

377 4 Discussion

378 In this paper we have introduced an original method to reconstruct the stiffness
379 distribution of the thoracic aorta from gated CT images considering ten phases of
380 a cardiac cycle. This methodology requires tracking the deformations of the aortic
381 wall throughout a cardiac cycle from the gated CT images. The deformations were
382 tracked without any additional information or marker indicating heterogeneous
383 deformation in between the bifurcations.

384 4.1 General remarks

385 For the first time ever, regional variations of stiffness properties across ATAA were
386 reconstructed on 3 patients non-invasively. To achieve this reconstruction, a novel
387 non-invasive inverse method was developed based on preoperative gated CT scans.
388 The non invasive identification of elastic properties of ATAA is highly important
389 as our research group [13, 48] recently showed that the membrane stiffness is sig-
390 nificantly correlated with the stretch based rupture risk of ATAA. Therefore, it
391 is significantly interesting to obtain the local membrane stiffness of the ascending
392 thoracic aorta to detect pathological regions with the highest risks of rupture. In-
393 terestingly, our results indicate that the local membrane stiffness is higher in the
394 aneurysmal ascending thoracic aorta than in the descending aorta, and that the
395 values are relatively higher than stiffness properties reported for healthy aortas.
396 However, despite this general trend, the distribution of membrane stiffness is het-
397 erogeneous in the aneurysmal region, with large stiffness in the bulging part of
398 aneurysm. The local loss of elasticity can be related to a more pronounced local
399 remodeling with, for instance, a larger fraction of collagen fibers. Sassani et al [43]

400 showed a large distribution of fiber orientations spanning from circumferential to
401 longitudinal directions, which was also supported by [46] stating that ATAA had
402 no effect on strength. However, this can cause stiffening and extensibility reduction,
403 corroborated with histological observation of elastin degradation but not collagen
404 content. It could be interesting also to check the possible correlation of these re-
405 gions with local concentration of wall shear stress induced by the blood flow [34].
406 All these possible correlations between regional variations of membrane stiffness
407 and local tissue composition or local hemodynamics effects are currently under
408 study in our group on a cohort of patients. Over the past decades the biomechan-
409 ical properties of the aorta have been widely investigated [7,50,21,40,18,12,25,
410 37,41,44]. As the aortic tissues are intrinsically anisotropic, the identified stiffness
411 provided by our method combines effects of the axial and circumferential exten-
412 sional linearized stiffness. However, as we use only the pressure loading to solve
413 the identification problem (we have no information on the axial tension in vivo),
414 it is dominated by effects of the circumferential extensional linearized stiffness.
415 This is in agreement with conclusions of Ferrara et al. [16] who indicated that the
416 weight of the circumferential elastic modulus is significantly higher than the weight
417 of the longitudinal one in the aortic mechanical response to pressure variations,
418 while there was no significant difference in the elastic modulus between anterior
419 and posterior regions in the longitudinal direction. The maximum circumferential
420 elastic modulus was reported in posterior region. Moreover, their results indicate
421 that regardless of age and gender, the mean elastic modulus is larger in the cir-
422 cumferential direction. However aging reduces the mean elastic modulus and male
423 has higher mean elastic modulus in comparison with female. Iliopoulos et al [30]
424 support these results and state that circumferential specimens were stiffer than
425 longitudinal ones in the posterior, left lateral, and all regions at physiologic and
426 high stresses but not at low stresses. Furthermore, in agreement with Ferrara et al.
427 [16] they found no significant regional variations of aortic stiffness in the circum-
428 ferential direction, and similarly at low stresses for longitudinal specimens, while
429 at physiologic and high stresses the right lateral was the stiffest ATAA region. In
430 the other study by the same group [29] it was shown that peak elastic modulus
431 in the anterior region was significantly lower than that in the right, but not the
432 left, lateral and posterior regions. Choudhury et al [7] studied local mechanical

433 properties of healthy and diseased, bicuspid and tricuspid aortic valves (BAV and
434 TAV), human ascending aorta. Indicating that BAV tissue was the thinnest and
435 contained the largest fraction of collagen, they found significantly less elastin both
436 in TAV and BAV tissue in contrast to healthy tissue, while on average the smallest
437 stiffness was observed in TAV patients. The elastic modulus was not dependent on
438 direction (isotropic) but it was dependent on the quadrant and tissue type. The
439 medial quadrant was the most compliant and the lateral quadrant tissue was the
440 stiffest.

441 Although most of these previous investigators carried out experimental tests on
442 tissue samples excised from patients during surgery, or on cadavers, the material
443 properties of tissues are commonly characterized averagedly across these samples
444 and in conditions which may be far from *in vivo* conditions, such as for instance
445 tensile test. Only recently, the use of digital image correlation (DIC) has made it
446 possible to investigate the local material properties of excised aortic samples [2,
447 11,10]. Inverse methods were developed to process DIC measurements and recon-
448 struct the regional variations of material properties, as for instance using a tension
449 inflation tests keeping the cylindrical shape of the aorta [4]. Regional variations of
450 constitutive properties make sense as they can be related to local tissue adaptation
451 through growth and remodeling [28].

452 When excised aortic samples are tested *in vitro*, the results usually take the
453 form of constitutive parameters in a strain energy density function [27]. Strain en-
454 ergy density functions usually have a large number of constitutive parameters with
455 possible couplings between each other and it was recently suggested to evaluate
456 more functional parameters, such as for instance the linearized *in vivo* stiffness
457 [4]. Here, we focused only on this linearized *in vivo* stiffness as we had only a
458 non invasive loading of the aorta across a limited range of strains through the
459 variations of blood pressure. The non invasive identification of the aortic stiffness
460 was previously achieved averagedly across aortic segments either by measuring the
461 aortic distensibility [48] or by measuring the pulse wave velocity [22], and relat-
462 ing these quantities to the aortic stiffness. Local non invasive identification was
463 previously achieved using 4D ultrasound on the abdominal aorta [32,51] but the
464 present study is the first one using gated CT scans and applying the approach
465 onto the ascending thoracic aorta. The availability of these images allowed us

466 to model subject-specific arterial configurations. Since a correlation between the
 467 stretch-based rupture risk and the tangent elastic modulus was found by [13],
 468 the methodology proposed here has potential to identify the rupture risk of aorta
 469 according to calculated local membrane stiffness.

470 It is important to point out the benefit of using a Fourier analysis (as done
 471 here for the regional reconstruction) instead of using simply diastolic and systolic
 472 geometries of the aorta (as done for distensibility measurements). Indeed, the dis-
 473 tensibility is usually assessed by measuring the change of cross section area of the
 474 aorta between diastole and systole, diastole being defined as the stage with mini-
 475 mum cross section area and systole being defined as the stage with maximum cross
 476 section area. **There is always a significant uncertainty on the times at which the 10**
 477 **phases of CT scans are acquired. If we could reduce this uncertainty and provided**
 478 **that a pressure curve can be measured simultaneously, the method could be easily**
 479 **extended to derive time variations of the stiffness throughout the whole cardiac**
 480 **cycle.** However, we noticed that locally, the maximum deflection of the aorta, and
 481 its maximum strains, are not reached at the same stage of the cardiac cycle de-
 482 pending on the position (Fig. 1). It means that the response of the aorta to the
 483 pressure variations presents phase shifts depending on the position. These phase
 484 shifts are potentially the result of viscous effect but also of the combined action of
 485 the blood pressure and of the cardiac motion, which are not synchronized, as this
 486 was previously shown by [52]. Due to these local phase shifts, it happens that the
 487 maximum strain of the aorta is not reached at systole for all the positions and the
 488 minimum strain of the aorta is not reached at diastole. Therefore, taking the aver-
 489 age change of strain between diastole and systole to derive the aortic stiffness, as
 490 done in the distensibility method [13, 48], automatically underestimates the actual
 491 strain variations occurring throughout a cardiac cycle. The consequence of this
 492 strain underestimation should be a stiffness overestimation for the distensibility
 493 method. However, in this work, it can be compensated by another effect which we
 494 would like to point out here as well. Commonly, pressure variations are linearly
 495 related to stress variations without considering the effects of radius variations as
 496 we did in Eq. 16. However, we found that the term considering the effects of ra-
 497 dius variations, namely $\frac{\tau_1^0(\Delta r_1)}{(r_1^0)^2} - \frac{\tau_2^0(\Delta r_2)}{(r_2^0)^2}$, is averagely responsible for about 10%
 498 of ΔP , with local effects possibly reaching 50%. Neglecting this term, as it is tra-

ditionally done in distensibility assessment, induces an underestimation of stress variations. Combined with the strain underestimation explained previously, the stress underestimation results in a good agreement of the distensibility method with our novel inverse method. Nevertheless, future stiffness identifications should take into account all these effects as done in the current study.

4.2 Limitations

There are several limitations in this work which can be discussed as below:

- The inverse approach is based on local equilibrium equations similar to the ones derived in [4]. These equations are obtained based on the principle of virtual work. It is worth noting that they are equivalent to the generalized Laplace’s law which writes the local equilibrium between pressures and tensions in a membrane. Accordingly, it means that it is assumed that the aortic wall behaves as a membrane with no bending moments or no through thickness shear. Regions near the branches may not satisfy the membrane assumption, and were removed from the analysis.
- The present study used gated CT scans as a source of dynamic images of the aortic wall during the cardiac cycle. The use of Xray may present a limitation for an extensive use of the methodology, especially if one wants to repeat the identification of aortic stiffness at different ages of ATAA growth, which would induce repeated irradiation for the patient. We are currently working on an extension of the method to images acquired with 4D MRI.
- The wall is assumed as a linearly elastic material within the systolic-diastolic range and we disregarded the layer-specific wall properties and residual stresses existing in the ATAA wall.
- We here assumed an isotropic behavior of the arterial wall. It was not possible to consider anisotropic effects as only one type of loading was available: variations of the blood pressure. The characterization of anisotropic materials requires loading samples in different directions. The consequence of the isotropy assumption in our approach is that the identified membrane stiffness is a combination of the axial and circumferential stiffness, which may be different. However, the local curvatures being involved in Eq. 17, most of the

- 530 weight is put on circumferential effects (the circumferential radius of curvature
531 being significantly lower than the axial one), meaning that the identified mem-
532 brane stiffness would be closer to the circumferential stiffness than to the axial
533 stiffness if there was a significant different between both.
- 534 – Average tensions existing in the aorta due to the action of the average blood
535 pressure are also involved in Eq. 17. This comes from geometrical nonlinearity
536 involved in finite deformations [3]. These tensions were approximated using the
537 approach of [32]. This approach consists in achieving a linear elastic stress anal-
538 ysis on the same structure as the aorta, assigning a very large elastic modulus.
539 The approach is valid for membrane structures. The membrane assumption
540 was previously shown to be a good approximation for elastostatics of aortic
541 aneurysms [33].
- 542 – Due to the removal of in vivo loadings, the artery experiences an elastic re-
543 coiling. Even when these loadings are removed, internal or residual stresses
544 still exist in the tissues. An effect of these internal stresses can be observed in
545 arteries with the well-known opening angle [38]. Moreover, Sokolis et al [45]
546 have provided evidence of residual stresses in both the circumferential and
547 longitudinal directions considering different wall layers of ATAA. Therefore,
548 disregarding the presence of residual stresses and considering the arterial wall
549 as a 3D membrane with uniform thickness can be considered as additional
550 limitations of the current work. Nevertheless, despite these limitations, the
551 structural membrane stiffness provided by our methodology is still a useful
552 indicator of local tissue altered remodeling.
- 553 – The segmented geometries have some local irregularities (bumps) due to image
554 noise at each phase of the cardiac cycle. The spatial frequency of these irregu-
555 larities is high and their effect is filtered out by Fourier polynomial smoothing.
556 However, if one wanted to obtain spatial variations of material properties with
557 a higher spatial resolution, one would have to address the issue of these geo-
558 metric irregularities.

5 Conclusion

Regional variations of stiffness properties across ATAA were reconstructed on 3 patients non invasively. To achieve this reconstruction, a novel non-invasive inverse method was developed based on preoperative gated CT scans. The non invasive identification of elastic properties of ATAA is highly important as our research group [13,48] recently showed that the membrane stiffness is significantly correlated with stretch based rupture risk of ATAA. It would be interesting in future studies to consider a cohort with a larger number of patients in order to interpret regional variations of stiffness properties in ATAAs in terms of local hemodynamics effects and of local tissue remodeling.

6 Acknowledgements

The authors are grateful to the European Research Council for grant ERC-2014-CoG BIOLOCHANICS.

7 Conflict of interest

The authors have no conflicts of interest to declare concerning the contents of this manuscript.

References

1. L. Antiga and D.A. Steinman. Robust and objective decomposition and mapping of bifurcating vessels. *IEEE Trans Med Imaging*, 23(6):704–13, 2004.
2. S. Avril, P. Badel, and A. Duprey. Anisotropic and hyperelastic identification of in vitro human arteries from full-field optical measurements. *Journal of biomechanics*, 43:2978–85, 2010.
3. S. Baek, R.L. Gleason, K.R. Rajagopal, and J.D. Humphrey. Theory of small on large: potential utility in computations of fluid–solid interactions in arteries. *Comput Methods Appl Mech Eng*, 196:3070–78, 2007.
4. MR. Bersi, C. Belliniand, P. Di Achille, J.D. Humphrey, K. Genovese, and S. Avril. Novel methodology for characterizing regional variations in the material properties of murine aortas. *Journal of biomechanical engineering*, 138:071005, 2016.

- 587 5. L.K. Bickerstaff, P.C. Pairolero, L.H. Hollier, L.J. Melton, H.J. Van Peenen, and
588 K.J. Cherry et al. Thoracic aortic aneurysms: a population-based study. *Surgery*, 92:1103-
589 08, 1982.
- 590 6. K.H. Chau and J.A. Elefteriades. Natural history of thoracic aortic aneurysms: size matters
591 and plus moving beyond size. *Prog Cardiovasc Dis*, 56(1):74-80, 2013.
- 592 7. N. Choudhury, B. Olivier, R. Leonie, T. Dominique, C. Raymond, and B. Jagdish et al.
593 Local mechanical and structural properties of healthy and diseased human ascending aorta
594 tissue. *Cardiovasc Pathol*, 18:83-91, 2009.
- 595 8. M.A. Coady, J.A. Rizzo, G.L. Hammond, G.S. Kopf, and J.A. Elefteriades. Surgical inter-
596 vention criteria for thoracic aortic aneurysms: a study of growth rates and complications.
597 *Ann Thorac Surg*, 67(6):1922-6, 1999.
- 598 9. M.A. Coady, J.A. Rizzo, G.L. Hammond, D. Mandapati, U. Darr, G.S. Kopf, and J.A. Elef-
599 teriades. What is the appropriate size criterion for resection of thoracic aortic aneurysms?
600 *J Thorac Cardiovasc Surg*, 113(3):476-91, 1997.
- 601 10. F.M. Davis, Y. Luo, S. Avril, Ambroise A. Duprey, and J. Lu. Local mechanical properties
602 of human ascending thoracic aneurysms. *Journal of the mechanical behavior of biomedical*
603 *materials*, 61:235-49, 2016.
- 604 11. FM. Davis, Y. Luo, S. Avril, A. Duprey, and J. Lu. Pointwise characterization of the elastic
605 properties of planar soft tissues: application to ascending thoracic aneurysms. *Biomechan-*
606 *ics and modeling in mechanobiology*, 14:967-78, 2015.
- 607 12. A. Duprey, K. Khanafer, M. Schlicht, S. Avril, D. Williams, and R. Berguer. In vitro
608 characterisation of physiological and maximum elastic modulus of ascending thoracic aortic
609 aneurysms using uniaxial tensile testing. *Eur J Vasc Endovasc Surg*, 39(6):700-7, 2010.
- 610 13. A. Duprey, O. Trabelsi, M. Vola, J.P. Favre, and S. Avril. Biaxial rupture properties of
611 ascending thoracic aortic aneurysms. *Acta Biomater*, 42:273-85, 2016.
- 612 14. T. McGloughlin (Ed.), editor. *Biomechanics and mechanobiology of aneurysms*. Springer-
613 Verlag, Heidelberg, 2011.
- 614 15. J.A. Elefteriades and E.A. Farkas. Thoracic aortic aneurysm clinically pertinent contro-
615 versies and uncertainties. *J Am Coll Cardiol*, 55(9):841-57, 2010.
- 616 16. A. Ferrara, S. Morganti, P. Totaro, A. Mazzola A, and F. Auricchio. Human dilated
617 ascending aorta: Mechanical characterization via uniaxial tensile tests. *J Mech Behav*
618 *Biomed Mater*, 53:257-71, 2016.
- 619 17. M.F. Fillinger, S.P. Marra, M.L. Raghavan, and F.E. Kennedy. Prediction of rupture risk
620 in abdominal aortic aneurysm during observation: wall stress versus diameter. *J Vasc*
621 *Surg*, 37(4):724-32, 2003.
- 622 18. Y.C. Fung. *Biomechanics. Mechanical properties of living tissues*. Springer, 1993.
- 623 19. C.M. García-Herrera, J.M. Atienza, F.J. Rojo, E. Claes, G.V. Guinea, D.J. Celentano,
624 C. García-Montero, and R.L. Burgos. Mechanical behaviour and rupture of normal and
625 pathological human ascending aortic wall. *Med Biol Eng Comput*, 50(6):559-66, 2008.

- 626 20. J.P. Vande Geest, E.S. Di Martino, A. Bohra, M.S. Makaroun, and D.A. Vorp. A
627 biomechanics-based rupture potential index for abdominal aortic aneurysm risk assess-
628 ment: demonstrative applicatio. *Ann N Y Acad Sci*, 1085:11–21, 2006.
- 629 21. J.P. Vande Geest, M.S. Sacks, and D.A. Vorp. Age dependency of the biaxial biomechanical
630 behavior of human abdominal aorta. *J Biomech Eng*, 126:815–22, 2004.
- 631 22. M. Groenink, A. de Roos, B.J. Mulder, J.A. Spaan, and E.E. van der Wall. Changes in aortic
632 distensibility and pulse wave velocity assessed with magnetic resonance imaging following
633 beta-blocker therapy in the marfan syndrome. *Am J Cardiol*, 82:203–8, 1998.
- 634 23. S. Haker, S. Angenent, A. Tannenbaum, and R. Kikinis. Nondistorting flattening maps and
635 the 3-D visualization of colon ct images. *IEEE trans. med. imaging*, 19:665–670, 2000.
- 636 24. Hibbit, Karlson, and Sorensen. *Abaqus-Theory manual*, 6.11-3 edition, 2011.
- 637 25. G.A. Holzapfel. Determination of material models for arterial walls from uniaxial extension
638 tests and histological structure. *J Theor Biol*, 238:290–302, 2006.
- 639 26. G.A. Holzapfel, T.C. Gasser, and R.W. Ogden. A new constitutive framework for arterial
640 wall mechanics and a comparative study of material models. *Journal of elasticity and the
641 physical science of solids*, 61 (1):1–48, 2000.
- 642 27. G.A. Holzapfel, T.C. Gasser, and R.W. Ogden. A new constitutive framework for arterial
643 wall mechanics and a comparative study of material models. *Journal of elasticity and the
644 physical science of solids*, 61(1-3):1–48, 2000.
- 645 28. J.D. Humphrey. Vascular adaptation and mechanical homeostasis at tissue, cellular, and
646 sub-cellular levels. *Cell Biochem Biophys*, 50:53–78, 2008.
- 647 29. D.C. Iliopoulos, R.P. Deveja, E.P. Kritharis, D. Perrea, G.D. Sionis, K. Toutouzas, C. Ste-
648 fanadis, and D.P. Sokolis. Regional and directional variations in the mechanical properties
649 of ascending thoracic aortic aneurysms. *Med Eng Phys*, 31(1):1–9, 2008.
- 650 30. D.C. Iliopoulos, E.P. Kritharis, A.T. Giagini, and D.P. Sokolis S.A. Papadodima. As-
651 cending thoracic aortic aneurysms are associated with compositional remodeling and ves-
652 sel stiffening but not weakening in age-matched subjects. *J Thorac Cardiovasc Surg*,
653 137(1):101–9, 2009.
- 654 31. G. Johansson, U. Markström, and J. Swedenborg. Ruptured thoracic aortic aneurysms: a
655 study of incidence and mortality rates. *J Vasc Surg*, 21(6):985–8, 1995.
- 656 32. G.R. Joldes, K. Miller, A. Wittek, and B. Doyle. A simple, effective and clinically appli-
657 cable method to compute abdominal aortic aneurysm wall stress. *J Mech Behav Biomed
658 Mater*, 58:139–48, 2016.
- 659 33. J. Lu, X. Zhou, and M.L. Raghavan. Inverse elastostatic stress analysis in pre-deformed bi-
660 ological structures: demonstration using abdominal aortic aneurysms. *J Biomech*, 40:693–
661 6, 2007.
- 662 34. P.G. Malvindi, S. Pasta, G.M. Raffa, and S. Livesey. Computational fluid dynamics of
663 the ascending aorta before the onset of type a aortic dissection. *European Journal of
664 Cardio-Thoracic Surgery*, 51(3):597–99, 2016.
- 665 35. C. Martin, W. Sun, T. Pham, and J. Elefteriades. Predictive biomechanical analysis of
666 ascending aortic aneurysm rupture potential. *Acta Biomater*, 9(12):9392–400, 2013.

- 667 36. G. Martufi, T.C. Gasser, J.J. Appoo, and E.S. Di Martino. Mechano-biology in the thoracic
668 aortic aneurysm: a review and case study. *Biomechanics and modeling in mechanobiology*,
669 13:917–928, 2014.
- 670 37. D. Mohan and J.W. Melvin. Failure properties of passive human aortic tissue. I-uniaxial
671 tension tests. *J Biomech*, 15:887–902, 1982.
- 672 38. S.J. Mousavi and S. Avril. Patient-specific stress analyses in the ascending thoracic aorta
673 using a finite-element implementation of the constrained mixture theory. *Biomech Model*
674 *Mechanobiol*, 16(5):1765–77, 2017.
- 675 39. S.J. Mousavi, S. Farzaneh, and S. Avril. Computational predictions of damage propagation
676 preceding dissection of ascending thoracic aortic aneurysms. *Int J Numer Method Biomed*
677 *Eng*, 34(4):e2944, 2017.
- 678 40. R.J. Okamoto, J.E. Wagenseil, W.R. DeLong, S.J. Peterson, N.T. Kouchoukos, and
679 T.M. Sundt 3rd. Mechanical properties of dilated human ascending aorta. *Ann Biomed*
680 *Eng*, 30:624–35, 2002.
- 681 41. P.J. Prendergast, C. Lally, S. Daly, A.J. Reid, T.C. Lee, and D. Quinn et al. Analysis
682 of prolapse in cardiovascular stents: a constitutive equation for vascular tissue and finite-
683 element modelling. *J Biomech Eng*, 125:692–99, 2003.
- 684 42. V.S. Ramanath, J.K. Oh, T.M. Sundt 3rd, and K.A. Eagle. Acute aortic syndromes and
685 thoracic aortic aneurysm. *Mayo Clin Proc*, 84(5):465–81, 2009.
- 686 43. S.G. Sassani, S. Tsangaris, and D.P. Sokolis. Layer- and region-specific material char-
687 acterization of ascending thoracic aortic aneurysms by microstructure-based models. *J*
688 *Biomech*, 48(14):3757–65, 2015.
- 689 44. D.P. Sokolis. Passive mechanical properties and structure of the aorta: segmental analysis.
690 *Acta Physiol (Oxf)*, 190:277–289, 2007.
- 691 45. D.P. Sokolis. Effects of aneurysm on the directional, regional, and layer distribution of
692 residual strains in ascending thoracic aorta. *J Mech Behav Biomed Mater*, 46:229–43,
693 2015.
- 694 46. D.P. Sokolis, E.P. Kritharis, A.T. Giagini, K.M. Lampropoulos, S.A. Papadodima, and
695 D.C. Iliopoulos. Biomechanical response of ascending thoracic aortic aneurysms: associa-
696 tion with structural remodelling. *Comput Methods Biomech Biomed Engin*, 15(3):231–48,
697 2012.
- 698 47. O. Trabelsi, F.M. Davis, J.F. Rodriguez-Matas, A. Duprey, and S. Avril. Patient specific
699 stress and rupture analysis of ascending thoracic aneurysms. *J Biomech*, 48(10):1836–43,
700 2015.
- 701 48. O. Trabelsi, M. Gutierrez, S. Farzaneh, A. Duprey, and S. Avril. A non-invasive
702 technique for ATAA rupture risk estimation. *Journal of Biomechanics*, page
703 doi.org/10.1016/j.jbiomech.2017.11.012, 2017.
- 704 49. EM. van Disseldorp, N.J. Petterson, MC. Rutten, FN. van de Vosse, MR. van Sambeek,
705 and RG. Lopata. Patient specific wall stress analysis and mechanical characterization of
706 abdominal aortic aneurysms using 4D ultrasound. *Eur J Vasc Endovasc Surg*, 52:635–42,
707 2016.

-
- 708 50. D.A. Vorp, B.J. Schiro, M.P. Ehrlich, T.S. Juvonen, M.A. Ergin, and B.P. Griffith. Effect
709 of aneurysm on the tensile strength and biomechanical behavior of the ascending thoracic
710 aorta. *Ann Thorac Surg*, 75:1210–14, 2003.
- 711 51. A. Wittek, K. Karatolios, P. Bihari, T. Schmitz-Rixen, R. Moosdorf, S. Vogt, and C. Blase.
712 In vivo determination of elastic properties of the human aorta based on 4D ultrasound
713 data. *J Mech Behav Biomed Mater*, 27:167–183, 2013.
- 714 52. A. Wittek, K. Karatolios, C.P. Fritzen, J. Bereiter-Hahn, B. Schieffer, R. Moosdorf,
715 S. Vogt, and C. Blase. Cyclic three-dimensional wall motion of the human ascending
716 and abdominal aorta characterized by time-resolved three-dimensional ultrasound speckle
717 tracking. *Biomech Model Mechanobiol*, 15(5):1375–88, 2016.

718 **List of Tables**

719	1	Demographic information of three patients. Note that ΔP is the	
720		difference between diastolic and systolic pressures, $Eh_{in-vivo}$ de-	
721		notes the extensional stiffness obtained by [48] and $Eh_{in-vitro}$ is	
722		the extensional stiffness obtained by [13].	29
723	2	Values of non-linear anisotropic material parameters for homoge-	
724		neous and heterogeneous models	29

Table 1 Demographic information of three patients. Note that ΔP is the difference between diastolic and systolic pressures, $Eh_{in-vivo}$ denotes the extensional stiffness obtained by [48] and $Eh_{in-vitro}$ is the extensional stiffness obtained by [13].

Patient ID	Sex	Age	ΔP [kPa](mmHg)	$Eh_{in-vivo}$ [MPa.mm]	$Eh_{in-vitro}$ [MPa.mm]
1	M	27	8.66 (65)	1.96	0.78
2	M	84	13.4 (100.5)	6.14	4.11
3	M	61	11.5 (86)	4.6	1.24

Table 2 Values of non-linear anisotropic material parameters for homogeneous and heterogeneous models

	C_{10} [kPa.mm]	k_1 [kPa.mm]	k_2	θ_1 [°]	θ_2 [°]
Homogenous	30	500	5	35	-35
Heterogeneous stiff	60	1000	5	35	-35
Heterogeneous compliant	30	500	5	35	-35

726 **List of Figures**

727 1 Segmentation of the aortic geometry for diastolic phase. Including
728 left subclavian artery, brachiocephalic artery, left common carotid
729 artery and coronary artery branches which are used as anatomical
730 references. See video 1 for ten phases of cardiac cycle. 32

731 2 It is assumed that each element of the arterial wall is a finite sector
732 of an ellipsoidal membrane with radii r_1 and r_2 in both circum-
733 ferential and longitudinal directions. n_1 and n_2 are tangential unit
734 vectors normal to r_1 and r_2 , respectively. n_i^n with $i=\{1,2,\dots,4\}$ is
735 normal unit vector at each node of the element. 33

736 3 Flowchart of the methodology to identify local membrane stiffness
737 of aorta. 34

738 4 Map of the displacement magnitude [mm] after inflation of the refer-
739 ence geometry (RG) using FE analysis considering a- a homogenous
740 stiffness and b- a heterogeneous stiffness distributions. 35

741 5 a- Displacement maps [mm] obtained by our methodology consid-
742 ering a homogenous stiffness, b- Reference displacement maps ob-
743 tained using a finite element analysis considering a homogenous
744 stiffness, c- Displacement maps obtained by our methodology con-
745 sidering a heterogeneous stiffness distribution, d- Reference dis-
746 placement maps obtained using a finite element analysis considering
747 a heterogeneous stiffness distribution. 36

748 6 Validation study: stiffness map [MPa.mm] reconstructed using our
749 methodology (left) for the assigned homogeneous stiffness (right)(a).
750 Stiffness map reconstructed using our methodology (left) for the as-
751 signed heterogeneous stiffness (right)(b). 37

752 7 Validation study: stiffness map [MPa.mm] reconstructed using our
753 methodology considering a- homogeneous and b- heterogeneous non-
754 linear anisotropic material properties. 38

755 8 Distribution of local membrane stiffness [MPa.mm] in ascending and
756 descending aortas for Patient 1 (a), Patient 2 (b) and Patient 3 (c).
757 Left and right show frontal and distal views respectively. 39

758	9	Distributions of local membrane stiffness [MPa.mm] for Patient 1	
759		(a), Patient 2 (b) and Patient 3 (c). Results in the left shows frontal	
760		and distal views of <i>in vivo</i> . Results in the right demonstrates <i>in vitro</i>	
761		cut.	40
762	10	Median and interquartile range of the local membrane stiffness [MPa.mm]	
763		obtained for <i>in vivo</i> cut, <i>in vitro</i> cut and whole ascending for Patient	
764		1 (a), Patient 2 (b) and Patient 3 (c). The blue and the red stars	
765		demonstrate the values of <i>in vivo</i> and <i>in vitro</i> cuts, respectively,	
766		which are calculated by [48] and [13].	41

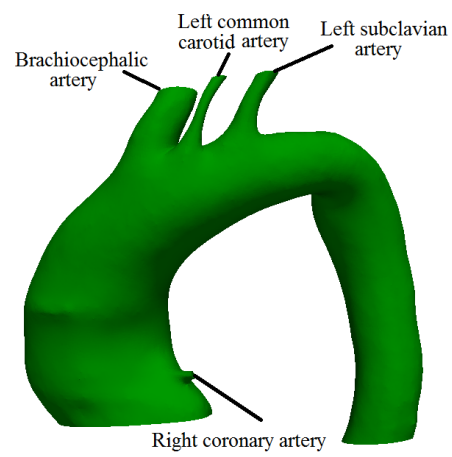


Fig. 1 Segmentation of the aortic geometry for diastolic phase. Including left subclavian artery, brachiocephalic artery, left common carotid artery and coronary artery branches which are used as anatomical references. See video 1 for ten phases of cardiac cycle.

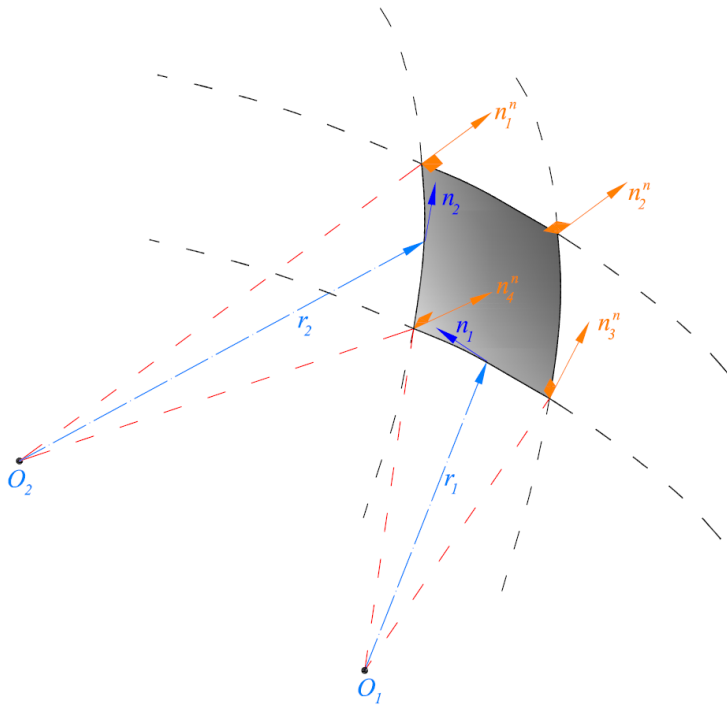


Fig. 2 It is assumed that each element of the arterial wall is a finite sector of an ellipsoidal membrane with radii r_1 and r_2 in both circumferential and longitudinal directions. n_1 and n_2 are tangential unit vectors normal to r_1 and r_2 , respectively. n_i^n with $i=\{1,2,\dots,4\}$ is normal unit vector at each node of the element.

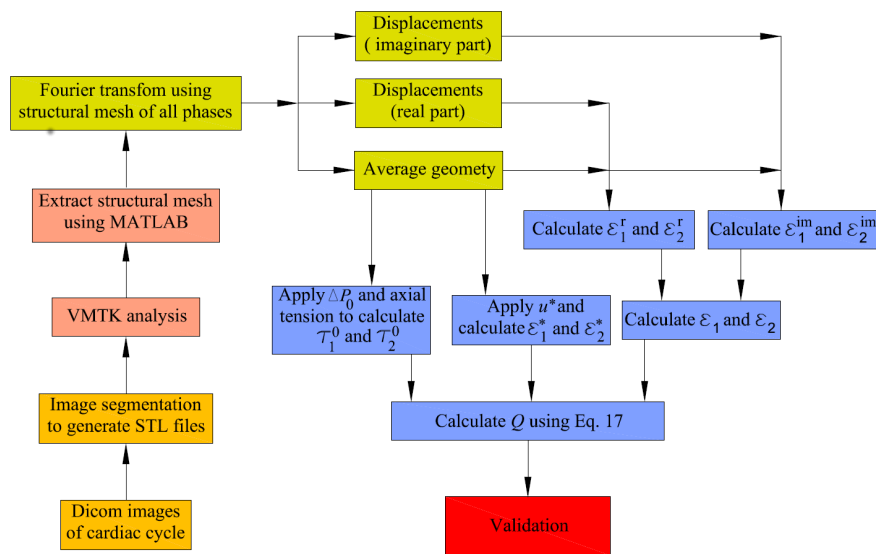


Fig. 3 Flowchart of the methodology to identify local membrane stiffness of aorta.

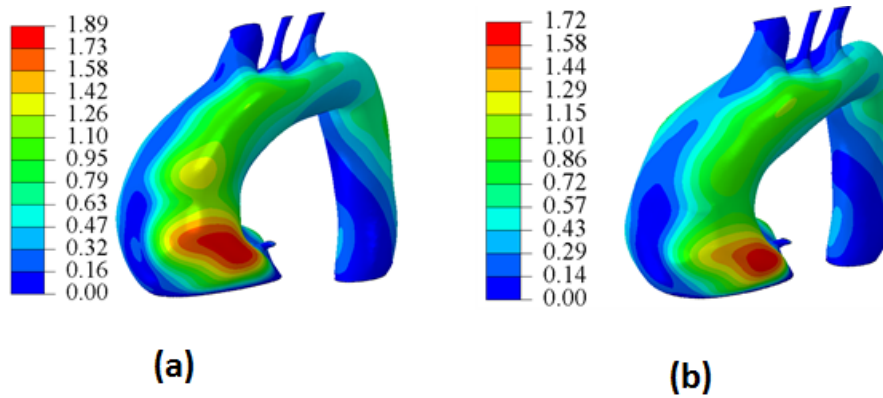


Fig. 4 Map of the displacement magnitude [mm] after inflation of the reference geometry (RG) using FE analysis considering a- a homogenous stiffness and b- a heterogeneous stiffness distributions.

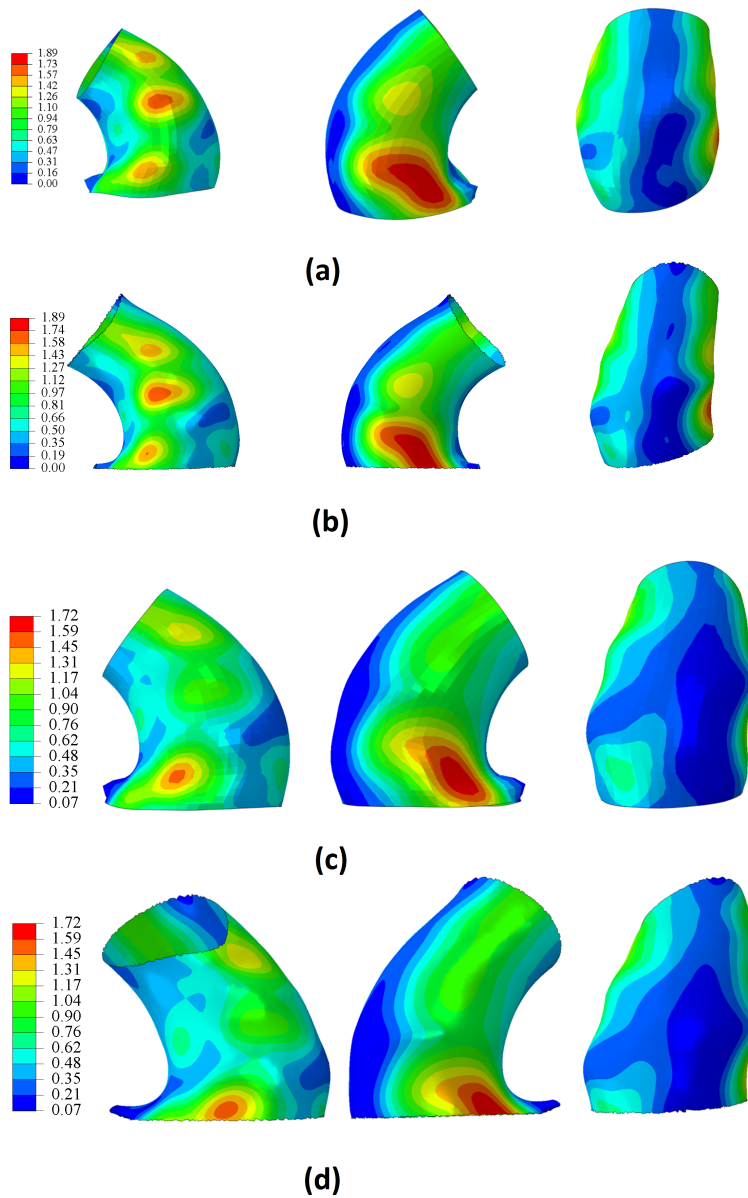


Fig. 5 a- Displacement maps [mm] obtained by our methodology considering a homogenous stiffness, b- Reference displacement maps obtained using a finite element analysis considering a homogenous stiffness, c- Displacement maps obtained by our methodology considering a heterogeneous stiffness distribution, d- Reference displacement maps obtained using a finite element analysis considering a heterogeneous stiffness distribution.

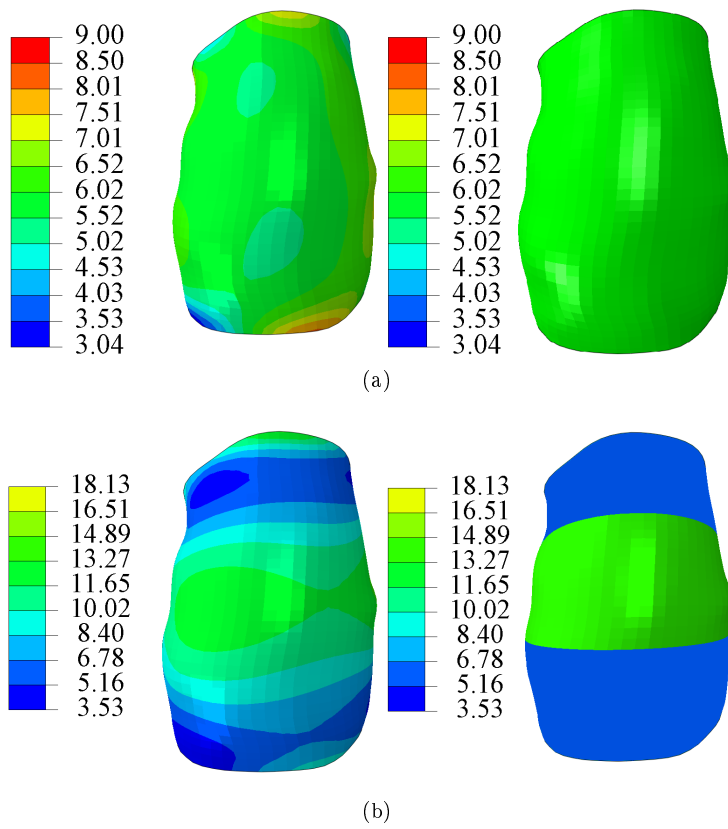


Fig. 6 Validation study: stiffness map [MPa.mm] reconstructed using our methodology (left) for the assigned homogeneous stiffness (right)(a). Stiffness map reconstructed using our methodology (left) for the assigned heterogeneous stiffness (right)(b).

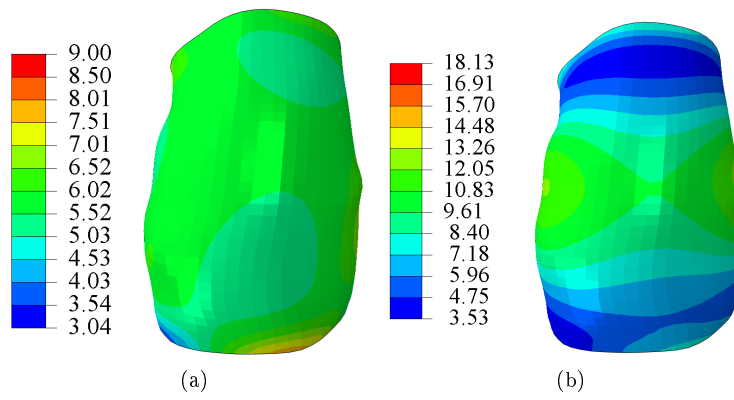


Fig. 7 Validation study: stiffness map [MPa.mm] reconstructed using our methodology considering a- homogeneous and b- heterogeneous non-linear anisotropic material properties.

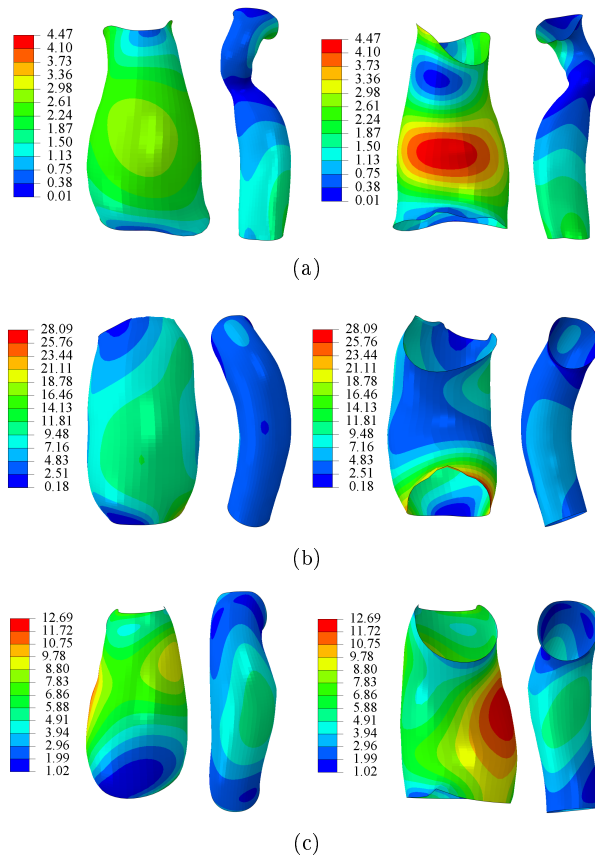


Fig. 8 Distribution of local membrane stiffness [MPa.mm] in ascending and descending aortas for Patient 1 (a), Patient 2 (b) and Patient 3 (c). Left and right show frontal and distal views respectively.

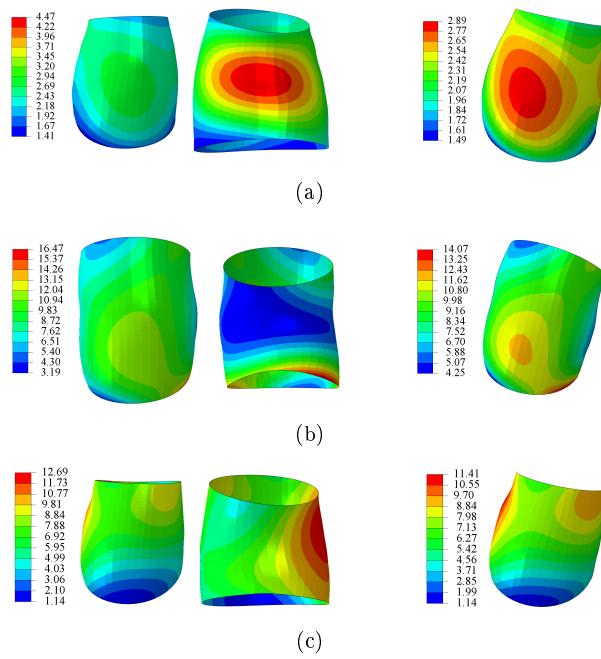


Fig. 9 Distributions of local membrane stiffness [MPa.mm] for Patient 1 (a), Patient 2 (b) and Patient 3 (c). Results in the left shows frontal and distal views of *in vivo*. Results in the right demonstrates *in vitro* cut.

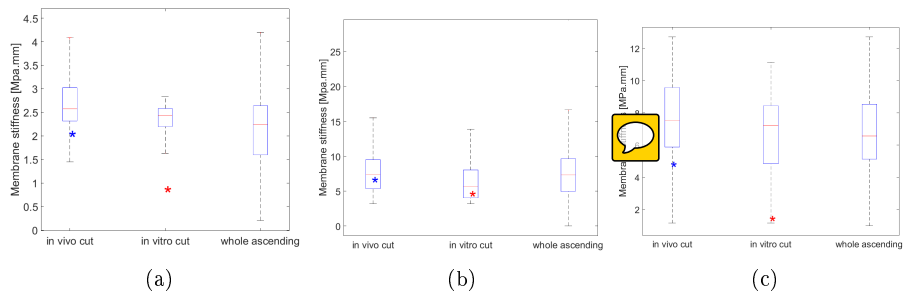


Fig. 10 Median and interquartile range of the local membrane stiffness [MPa.mm] obtained for *in vivo* cut, *in vitro* cut and whole ascending for Patient 1 (a), Patient 2 (b) and Patient 3 (c). The blue and the red stars demonstrate the values of *in vivo* and *in vitro* cuts, respectively, which are calculated by [48] and [13].